Research Square

Preprints are preliminary reports that have not undergone peer review.
They should not be considered conclusive, used to inform clinical practice,
or referenced by the media as validated information.

Swell application reveals and quantifies wavefront propagation of halorhodopsin-induced spreading depolarization

Clayton Dunford
Brigham Young University
Preston C. Withers
Brigham Young University
Dallin S. Nevers
Brigham Young University
T. Luke Shafer
Brigham Young University
R. Ryley Parrish
ryley_parrish@byu.edu

Brigham Young University

Method Article

Keywords: Spreading depression, intrinsic optical imaging, intrinsic optical signal, open-source tools, optogenetics

Posted Date: November 4th, 2026

DOI: https://doi.org/10.21203/rs.3.rs-10856711/v1

License: This work is licensed under a Creative Commons Attribution 4.0 International License.
Read Full License

Additional Declarations: No competing interests reported.

Abstract

Background

Spreading depolarization (SD) is the cellular correlate of migraine aura and often occurs during brain injury and seizures. SD can be experimentally induced by multiple methods, including elevated extracellular K^+ and emerging optogenetic paradigms employing either channelrhodopsin or halorhodopsin (HaloR). Interestingly, HaloR-induced SD can arise while neurons are hyperpolarized and extracellular K^+ is below baseline, conditions opposite to conventional induction; however, consistent propagation of these events has not been established. Intrinsic optical signal (IOS) imaging has long been used to track SD propagation, but no dedicated user-friendly open-source tools exist for SD event characterization validated across traditional and optogenetic induction.

Methods

Here, we present Swell, a desktop application for identifying and quantifying SD-associated IOS. Experiments used *ex vivo* brain slices from male and female C57BL/6 and HaloR × EMXCre mice. Swell was first validated with SD events induced by elevated extracellular K^+, comparing its output with electrophysiology data and manual SD segmentation. Swell was then used to characterize HaloR-induced SD, and event metrics were compared to those of elevated extracellular K^+-induced events. Analyses used nonparametric methods with percentile cluster-bootstrap confidence intervals.

Results

Swell-derived IOS arrival was coincident with direct current electrophysiology deflection (bias − 0.2 s, 10/10 events within 3 s); its generated masks matched those produced by trained human annotators (Dice 0.92 vs. inter-annotator 0.92); and exported propagation speed fell within published values. Swell was used to demonstrate that HaloR-induced SD events propagate beyond the induction site both during and following illumination, at speeds similar to those triggered by elevated extracellular K^+.

Conclusions

Swell is a validated open-source desktop application for quantifying SD. Applied across paradigms, Swell revealed that SD initiated during HaloR illumination propagate at speeds that do not detectably differ from those induced by elevated extracellular K^+, demonstrating that HaloR-induced SD propagate consistently following their induction and that optogenetically triggered SD can be reliably tracked with IOS. These findings further validate HaloR as an SD induction model whose unique extracellular conditions offer promising potential to decouple the mechanisms of SD induction from propagation.

1 Background

Spreading depolarization (SD) is a near-complete neuronal and glial depolarization that propagates through central nervous system tissue at a rate of 2–9 millimeters per minute [1]. Discovered in 1944 [2], SD has since been implicated in a variety of neuropathologies including migraine with aura [3–5], seizure [6–8], traumatic brain injury [9–11], and stroke [12–14]. Despite its clinical significance, the mechanisms of SD propagation are incompletely understood, remaining an active focus in neuroscience research [15]. SD can be experimentally induced in animal models through several techniques, commonly via mechanical injury [16–18], hypoxia [19–22], ischemia [23–25], and elevated extracellular K^+ [26–29].

In recent years, the optogenetic protein channelrhodopsin has been used as a method to induce SD without directly altering the extracellular environment [30–32]. Our lab has also demonstrated that SD can be consistently induced using the optogenetic tool halorhodopsin (HaloR), which hyperpolarizes neurons and subsequently reduces extracellular K^+ below baseline [33]. Using HaloR, SD events can occur after illumination, as accumulated KCl is extruded from the neurons and extracellular K^+ starts to rebound, but they can also occur in a more unexpected manner, during illumination itself when extracellular K^+ is below physiological levels [33, 34]. HaloR-induced SD can therefore be used to clearly decouple elevated extracellular K^+ from SD induction and potentially tease apart possible mechanistic differences between induction and propagation. However, whether HaloR-induced SD propagate consistently after initiation remains unknown, a critical consideration for establishing this paradigm as a tool for investigating the mechanistic underpinnings of SD.

SD has historically been identified by its negative direct current (DC) voltage shift in electrophysiology recordings [2, 35], whose spatial resolution is limited by the number of electrodes and their placement in the tissue. SD also drives osmotic shifts that swell cells, altering how the tissue scatters light [1]. These scattering changes, known as intrinsic optical signals (IOS), arise concurrently with the DC shift [19, 36], allowing SD events to be detected and spatially characterized through IOS imaging (IOSI), which has substantially advanced the study of SD propagation [20, 37–39]. Because electrophysiology resolves timing precisely at discrete sites while IOSI resolves the wavefront across the tissue, the two are often used together [40]. Analysis tools, however, have not kept pace. Although custom programs have been developed for general IOS identification, isolation, and analysis [41, 42] or for calculating select IOS parameters such as signal velocity and trajectory using *in vivo* rodent models [43], no dedicated open-source tools have previously been developed for comprehensive SD-associated IOS analysis.

Here, we present Swell, a desktop application that identifies, segments, and quantifies SD from IOSI, developed and validated using *ex vivo* rodent models [44]. Swell combines semi-automated event detection, interactive wavefront segmentation with a foundation image segmentation model, Segment Anything Model 2.1 (SAM 2.1) [45], and metric export into a single pipeline, enabling users to characterize SD event metrics including optical intensity, propagation speed, area recruited, and relative area recruited. We benchmarked Swell-derived event detection against manually identified events, and validated IOS arrival timing against simultaneous electrophysiological recordings during SD induced by

perfusion with elevated extracellular K^+. Furthermore, we compared Swell-generated wavefront masks against those drawn by trained annotators, finding them equivalent to manual annotation.

We used Swell to analyze HaloR-induced SD. Prior HaloR work relied on electrophysiology alone, in both *in vivo* and *ex vivo* models [33] and did not establish whether these events consistently propagate, a defining feature of SD [1, 2]. We captured SD occurrence with IOSI and electrophysiology to demonstrate that these events propagate regularly beyond their initiation site, recruiting tissue across the neocortex. We also found similar SD propagation speeds between elevated extracellular K^+-induced events and HaloR-induced events occurring both during and after illumination, further validating the use of HaloR as an SD induction paradigm.

Swell provides a validated, open-source route to quantifying and comparing SD across induction paradigms, allowing for the coupling of optogenetics, electrophysiology and IOS into the same experiment. Applying it to HaloR-induced SD events shows they propagate normally even when initiated with extracellular K^+ below baseline levels, separating the conditions that initiate SD from the resulting wavefront.

2 Methods

2.1 Animals

Two mouse lines were used. Wild-type C57BL/6 mice were used for elevated extracellular K^+ SD induction. HaloR × EMXCre mice, whose neocortical pyramidal cells expressed eNpHR3.0, were used for optogenetic SD induction and elevated extracellular K^+ SD induction experiments. Wild-type C57BL/6 mice were bred in-house. HaloR × EMXCre mice were generated by cross-breeding homozygous Emx1-cre mice [46] (The Jackson Laboratory, stock #005628) with mice containing a floxed STOP cassette in front of an eNpHR3.0/EYFP domain (The Jackson Laboratory, stock #014539). A total of 17 male and female mice between the ages of 4 and 12 weeks (28–85 days) were included in this study. Animals were group-housed under a 12-hour light/dark cycle with *ad libitum* access to food and water, with a minimum of two enrichment items per cage. All procedures were performed in accordance with Brigham Young University Institutional Animal Care and Use Committee (IACUC) guidelines.

2.2 Slice Preparation

C57BL/6 and HaloR × EMXCre mice were anesthetized using isoflurane prior to decapitation. The brains were removed, and a Leica 1200S vibratome was used to prepare horizontal slices with a thickness of 400 µm while the brains were submerged in ice-cold cutting solution containing (in mM): 126 NaCl, 3.5 KCl, 26 $NaHCO_3$, 1.26 NaH_2PO_4, 3 $MgCl_2$, 10 glucose. Slices were then bilaterally severed with a scalpel along the optic tract and extending through the dorsolateral orbital cortex, retaining the sections lateral to the cuts (Fig. 1A). For elevated extracellular K^+ experiments, additional cuts were made through the secondary somatosensory cortex to further reduce the size of the slice. The larger sections were used

for HaloR experiments to better observe potential propagation beyond the area obscured by the activation light. All sections, which contained the hippocampus, striatum, and much of the neocortical tissue, were then temporarily placed in a custom submersion holding chamber [47] filled with artificial cerebrospinal fluid (aCSF) containing (in mM): 126 NaCl, 3.5 KCl, 26 $NaHCO_3$, 1.26 NaH_2PO_4, 2 $CaCl_2$, 1 $MgCl_2$, 10 glucose. After all of the slices had been sectioned and placed in the submersion holding chamber, slices were then transferred to a custom-made interface holding chamber [48] containing aCSF for an acclimation period of at least one hour prior to experimentation.

2.3 Spreading Depolarization Induction

Experiments were performed using a custom-made interface recording chamber, in which slices were perfused with aCSF heated to 34–37°C (Fig. 1B). For experiments utilizing elevated K^+ to induce SD, an Isotemp 3016HS heater (Fisher Scientific) was used to warm the aCSF solution, and slices were perfused at a rate of 3.0–4.0 mL/min using a PPS2 pump (Multi Channel Systems). For all other experiments, a recirculating chiller (Vevor) was used to warm the solution, and aCSF was perfused across the slice at a rate of 3.0–4.0 mL/min with a Minipuls 3 peristaltic pump (Gilson).

2.3.1 Potassium-induced Spreading Depolarizations

Elevated extracellular K^+ aCSF solutions were prepared by increasing the KCl concentration to 15 mM or 26 mM, replacing NaCl on an equimolar basis (to 114.5 and 103.5 mM, respectively), with all other components as in the standard aCSF described in 2.2. After a minimum 10-minute equilibration period on the interface recording system, mouse brain slices were subjected to one of two experimental paradigms.

For the 15 mM K^+ aCSF paradigm, slices were perfused with 15 mM K^+ aCSF for 40 minutes, during which period 1–7 SD events were observed in each slice. Following the 40-minute 15 mM K^+ paradigm, the perfusion was then switched to 26 mM K^+ aCSF for 7 minutes before returning to perfusion with standard aCSF. The resulting SD events induced with 26 mM K^+ were only used to tune Swell's automated detection algorithm.

For the independent 26 mM K^+ aCSF paradigm, the slices were perfused with 26 mM K^+ aCSF until SD was observed or for a maximum of 7 minutes. Upon confirmation of SD onset, perfusion was immediately reverted to standard aCSF. As with the previous 26 mM paradigm, the resulting SD events were used exclusively for automated detection tuning.

2.3.2 Halorhodopsin-induced Spreading Depolarizations

To facilitate optogenetic HaloR activation, an LEDD1B driver (ThorLabs) emitting 565 nm light was coupled to an optic fiber positioned adjacent to the neocortex of a HaloR × EMXCre slice near the recording electrode [33]. Initially, the light was turned on at the maximum intensity for a duration of 90

seconds. If the first attempt failed to induce SD, the duration was increased up to 300 seconds in subsequent induction attempts. SD events occurred either during light stimulation or immediately thereafter. If an SD occurred during illumination, the light was left on for at least an additional 90 seconds to avoid distorting imaging of SD-associated IOS. Following each induction attempt, slices were allowed to rest for at least the duration of the preceding light stimulation. This amounted to 90 seconds after the initial induction attempt and at least 300 seconds after each subsequent attempt.

2.4 Electrophysiology Recordings

To obtain DC recordings, 1 MΩ micropipettes were pulled using a P-87 Flaming/Brown Micropipette Puller (Sutter Instruments Co.) from GC120TF-10 borosilicate glass capillaries (Harvard Apparatus), backfilled with standard aCSF, mounted on a headstage, and inserted approximately 200 μm into the neocortex of the brain slices. A chlorinated silver wire secured to the interface recording chamber in the perfused recording solution served as a reference electrode. The DC signal was sampled at 10,000 Hz, amplified 10 times using a custom-built amplifier, digitized with an NI USB-6341 X Series Multifunction DAQ board (National Instruments), and recorded using WaveSurfer 1.0.6 [49] running in MATLAB 2024b.

2.5 IOS Recordings

During elevated extracellular K^+ experiments, IOS were captured using a DAGE-MTI IR-2000 microscope camera (DAGE-MTI, Michigan City, IN) at 3072 × 2048 pixel resolution with 8-bit RGB color images and gain ranging from 1× to 3×. For HaloR-induced SD experiments, IOS were captured using a Lumenera INFINITY8-2M microscope camera (Teledyne Vision Solutions, Thousand Oaks, CA) at 1608 × 1104 pixel resolution with 8-bit grayscale images and gain set to 1×. Camera exposure was 1–5 ms for both systems. Differing cameras and recording settings were intentionally selected to assess and demonstrate pipeline generalizability and normalization. The cameras were mounted on AmScope SM-6 Series zoom trinocular stereo microscopes (AmScope, Irvine, CA) at 1× magnification, positioned approximately 12 cm above the interface chamber. The pixel-to-mm ratio was calibrated for each slice using a reference of known dimensions or the measured length of the cortical slice long axis (Fig. 2D).

Slice illumination was provided by a battery-powered gooseneck LED work light at full power (Harbor Freight, Calabasas, CA) and used in all paradigms to ensure even lighting across the brain slices. The light was positioned above the slice next to the camera to enable the camera to capture changes in slice reflectance. Recordings occurred at a native temporal resolution of 1 Hz for the duration of the experiment and were stored as uncompressed Tag Image File Format (.TIFF) sequences.

2.6 Swell Analysis Pipeline

Swell processes image sequences through a four-stage pipeline. Image frames are read into the application (Fig. 2A), with color frames converted to grayscale by averaging the RGB channels. Events are then identified either manually, using the frame viewer and marking event start and end frames, or automatically (2.6.1). They are then preprocessed, segmented, and quantified (Fig. 1C).

2.6.1 Automated SD Detection

Swell detects SD events from image stacks using an automated algorithm on a user-defined region of interest (ROI) (**Fig. 1Ci**). Prior to the detection itself, images used by the detector that are larger than 800 pixels on the long axis are downsampled so that the long axis is 800 pixels, with the aspect ratio preserved, and cropped to the bounding box of the user-defined ROI (Fig. 2C). The bounding box is partitioned into a 40 × 40 grid of subsections (default; user-adjustable), each of which is intersected with the ROI; subsections containing no ROI pixels are removed (Fig. 2B). For each subsection, an optical intensity trace is computed from the lower median pixel values, suppressing bright specular reflections. Each trace is subsequently detrended to remove slow baseline drift.

Following intensity extraction, detection proceeds in two stages. In Stage 1, candidate events are generated as time windows of coordinated subsection activity. For each detrended trace, the frame-to-frame difference is computed, and a per-subsection noise scale is estimated as the median absolute deviation (MAD) of the difference signal. A subsection is marked active at frames where its derivative exceeds 2.5 × MAD. By default, the detector responds to positive deflections, as the primary optical signal associated with SD is an increase in light scattering and therefore an increase in reflectance [36, 50]. Detection polarity is configurable for transmittance-based imaging. The number of active subsections per frame is then summed, smoothed (window = 10 frames), and analyzed for peaks with a minimum height of 5% of retained subsections and a minimum separation of 50 frames. Around each peak, the event window is expanded (up to 150 frames before and 250 frames after the peak) until activity returns below a quiet baseline of 1% of retained subsections; each window is recorded as a candidate event. Candidate events 40 frames or shorter are discarded. Finally, broad windows containing separable recruitment episodes are conservatively split into up to 3 segments using the newly-active-subsection signal.

Stage 2 applies a coherence gate: each Stage 1 candidate is scored for temporal coherence of subsection recruitment. For each subsection, a noise scale is calculated as the MAD of subsection's detrended intensity trace over the 200 seconds immediately preceding the candidate window. Values within the candidate window are divided by this scale, and subsections with MAD-normalized values exceeding 10 were marked active. The number of active subsections per frame is then calculated and its lag-1 autocorrelation is used as the coherence score. Candidates scoring below the operating threshold (a coherence score of 0.826) are rejected. The operating threshold was selected by maximizing the F1 score. During leave-one-animal-out evaluation, the operating threshold was re-tuned on each training fold, ensuring that the reported precision and recall were not obtained at a threshold fitted to the held-out data.

2.6.2 Event Preprocessing

Prior to segmentation, events undergo a three-step preprocessing pipeline (**Fig. 1Cii**). Events are smoothed using a 2D Gaussian blur (σ = 0.5). A baseline is then calculated as a pixelwise median from up to 30 frames prior to the event initiation. When fewer than 30 frames are available, the maximum

number of viable frames is used. Following its calculation, the baseline is subtracted from the rest of the event images. Finally, to increase contrast, the 1st – 99th percentiles are computed across the stack. Each frame is clamped to that range then rescaled to 0–255.

2.6.3 Segmentation and Propagation

Event segmentation is performed using the SAM 2.1 Hiera Base+ Video Predictor [45] on the event frames (**Fig. 1Ciii**). The user places point prompts (positive or negative), box prompts, and/or brush edits on anchor frames to define the initial and final wavefront masks (Fig. 2E). Propagation is run bidirectionally over a user-selected range from the nearest anchor frame. The user can then inject additional prompts or modify existing masks and re-run the propagation segmentation. After event segmentation is completed, the output is saved as binary masks — one per frame, labeling each pixel as inside or outside the wavefront.

2.6.4 Metric Extraction

Prior to metric extraction, the ROI and scaling are defined (Fig. 2C,D) and saved binary masks are intersected with the ROI, keeping only the area of the masks that fall inside of the ROI. For each slice, the ROI was limited to the neocortical region of the brain slice. SD events initiated during HaloR activation via 565 nm illumination were partially obscured by the intense light. In these cases, the ROI was drawn to exclude the area blocked by the light.

Using the binary masks and the user-defined ROI (Fig. 2C), baseline, pixel-to-mm scale (Fig. 2D), and frame interval, Swell generates four primary frame-by-frame and summary metrics. Intensity ($\Delta I/I_0$) is computed over the ROI; propagation speed (μm/s), area recruited (mm²), and relative area recruited (%) are derived from the segmented boundary (**Fig. 1Civ,Cv**). For each mask, holes are filled, and only the largest contiguous region is retained. The resulting boundary is then smoothed with a fast Fourier transform-based low-pass filter using a 25-component frequency cutoff to reduce noise.

Intensity is reported as $\Delta I/I_0$, the fractional change in mean ROI brightness from baseline. For each frame, pixel values within the ROI are spatially averaged; the baseline is the mean of these averages across the baseline frames, and each event frame's average is baseline-subtracted and divided by it.

Propagation speed is calculated per frame as the average outward displacement of the wavefront boundary relative to the previous frame's boundary, computed only on boundary points advancing more than 15 μm. Frames with no points that meet that threshold are flagged for user review and, for the data reported here, were treated as zero-speed frames. Displacements are converted to μm/s using the pixel-to-mm scale and the frame interval. Average propagation speed is generated by taking the average of the frame-by-frame propagation speeds.

Area recruited is calculated by converting the per-frame area enclosed by the smoothed boundary into mm² using the pixel-to-mm scale. Maximum area recruited is generated by taking the maximum of the per-frame areas during the event.

Relative area recruited is calculated by dividing the per-frame area enclosed by the smoothed boundary by the pixel count of the ROI and multiplying by 100 to convert to a percentage. Maximum relative area recruited is generated by taking the maximum of the per-frame relative areas during the event.

2.7 Detector Evaluation

Detector performance was evaluated separately from the output validation described in 2.8, using SD events induced by 15 mM or 26 mM elevated extracellular K^+ in standard aCSF (n = 27 events / 10 slices / 7 animals). Ground truth was the set of SD events identified by the authors from the image stacks, confirmed by the characteristic DC shift where simultaneous electrophysiology was available. Detector windows were matched to these events by temporal overlap: each event with at least one accepted detector window was counted once as a true positive, accepted windows matching no identified event were counted as false positives, and identified events with no accepted window were counted as false negatives. Precision and recall were evaluated by leave-one-animal-out cross-validation. In each fold, all recordings from one animal served as the held-out test set, while recordings from the remaining animals formed the training set used to select the Stage 2 threshold (2.6.1). Predictions from the held-out animals were then pooled to calculate overall precision and recall.

2.8 Validation

Swell outputs were validated in three ways: event timing against simultaneous DC recordings, segmentation fidelity against manual expert masks, and derived metrics against published SD ranges. Validation used manually identified 15 mM elevated extracellular K^+-induced SD events with a single initiation site. The 15 mM K^+ validation cohort comprised 10 events from 4 slices in 2 animals, with 7 out of 10 events coming from one slice and 8 out of 10 from one animal.

DC and IOS recordings were synchronized so that timing could be compared directly. Event onset was determined by the first frame containing a non-empty segmentation mask and served as the time reference for each event. The electrode ROI was a 100 × 100 pixel box centered around the recording electrode tip with the area occluded by the electrode subsequently removed (Fig. 4A). IOS arrival was determined as the first frame in which the segmented mask intersected with the electrode ROI, and the DC shift as the manually identified DC deflection characteristic of SD. Both were expressed relative to event onset.

Segmentation accuracy was assessed against manual expert masks. For each of 10 events, 8 frames were selected at approximately equal intervals between the first and last frames containing a non-empty Swell mask, thereby spanning the event's full detected active period. The corresponding preprocessed images were independently segmented using manually drawn masks by three trained annotators, blinded to each other and to the Swell output. All masks were restricted to the tissue ROI. For each frame, a manual consensus mask was constructed by pixelwise majority vote, with a pixel included when marked by at least two of the three annotators. Agreement between the Swell mask (S) and the manual consensus mask (C) was calculated using the Dice coefficient, $2|S \cap C| / (|S| + |C|)$. Inter-annotator

agreement was calculated using the same coefficient for each of the three annotator pairs and averaging the three pairwise values. The 8 frame-level Swell-versus-consensus and inter-annotator values were then averaged separately to obtain one value of each measure per event. Average propagation speed was extracted as described in 2.6.4 and compared to published *ex vivo* ranges.

2.9 Cross-Paradigm SD Characterization

Manually identified events were classified by induction method (elevated extracellular K^+ or HaloR activation). HaloR events were further classified by SD onset timing relative to illumination: onset during 565 nm illumination was classified as during illumination, and onset within the 30 s following illumination as post-illumination. Events with onset more than 30 s after illumination ended (before any subsequent illumination), that occurred in the hippocampus, or with initiation sites outside the directly illuminated area were excluded from cross-paradigm SD characterization.

Each SD event confirmed via a manually identified DC shift (recorded from an electrode placed within the 565 nm illuminated area) was scored as being IOS-detected if a propagating IOS wave was visible within the neocortical ROI in manual review. Detection concordance was reported as the proportion of DC-confirmed events that were also detected by IOS, separately for during- and post-illumination events. Events detected by IOS without a corresponding DC shift were excluded from the concordance denominator and tabulated separately as IOS-only detections. Metric analyses used IOS-detected events regardless of DC confirmation.

Propagation speed was extracted as described in 2.6.4 for events with a single initiation site, regardless of DC confirmation, and compared across during-illumination, post-illumination, and elevated extracellular K^+-induced events (same elevated K^+ cohort as used in 2.8). Intensity was excluded from analysis due to the large light fluctuations that occur during HaloR activation. Maximum absolute and relative neocortical area recruitment measures were excluded from analysis due to differences in slice preparation between paradigms (2.2), confounding from the variation in size and location of illumination, and obscured area from the light itself. Analysts were not blinded to induction paradigm, as the illumination used for HaloR induction is visible in the recordings.

2.10 Statistical Analysis

Sample sizes are reported as events/slices/animals throughout. No a priori sample size calculation was performed; sample sizes were determined by the number of recordings available. Events from male and female mice were pooled; sample sizes were not designed to detect sex differences.

Confidence intervals were obtained by percentile cluster bootstrap with 10,000 iterations, resampling the unit that accounts for repeated measures in each analysis: animals for detector evaluations (2.7), and slices for output validation (2.8) and cross-paradigm characterization (2.9). Timing agreement is reported as the bias (IOS – DC) with this cluster-robust CI. Differences between paradigms are reported as the observed differences in medians (HaloR – elevated K^+), with slices resampled independently

within each group. Maximum relative neocortical area recruited and cross-paradigm comparisons are reported descriptively without formal equivalence testing.

Analyses were performed in Python using NumPy [51] and SciPy [52]. Nonparametric methods were used throughout. Generative AI (Anthropic Claude Code, OpenAI Codex) was used to assist in drafting portions of the Python code for the Swell application and the statistical analyses. All AI-assisted code was reviewed and tested by the authors; the authors executed the analyses, verified the resulting outputs, and take responsibility for the software and analytical results.

3 Results

3.1 Automated SD Detection

Swell's two-stage detector identified SD events in elevated extracellular K^+ recordings (Fig. 3). An SD event appears in the detector as many subsections activated in unison as the wavefront crosses the ROI (Fig. 3A).

The detector uses a two-stage system to uncover the low signal intensity changes associated with SD and separate them from general noise. Stage 1 is highly sensitive, detecting 25 out of 27 true events but admitting 49 false positives across the dataset (Fig. 3B,C), a precision of 0.34 (95% CI [0.23, 0.53]). Because true SD events recruit subsections in a temporally coherent manner, Stage 2 serves as a coherence gate to Stage 1, retaining 24 out of 25 true events previously detected while rejecting 43 out of 49 false positives (Fig. 3C,D).

Across elevated extracellular K^+-induced SD events (n = 27 events / 10 slices / 7 animals), the detector achieved a precision of 0.80 (95% CI [0.73, 0.90]), a recall of 0.89 (95% CI [0.82, 0.96]), and an F1 score of 0.84 (95% CI [0.81, 0.89]), evaluated by leave-one-animal-out cross-validation, with CIs generated from cluster bootstrap across animals (Fig. 3D). When separated by extracellular K^+ concentration, the precision and recall scores demonstrate that the detector performs similarly across 15 mM (precision: 0.85, recall: 0.85) and 26 mM (precision: 0.76, recall: 0.93) concentrations. Detection alone does not establish that the resulting measurements are accurate.

3.2 Swell Validation

Swell event timing, segmentation, and derived metrics (n = 10 events / 4 slices / 2 animals) were accurate when compared against electrophysiology data, expert annotation, and the literature (Fig. 4A–F).

IOS arrival in the Swell masks was essentially coincident with the electrophysiological DC shift (Fig. 4B). No systematic offset was found (bias − 0.2 s, slice-clustered 95% CI [− 2.2 s, + 0.3 s]), and 10/10 IOS arrivals fell within 3 s of the DC shift with a median absolute difference of 1 s (Fig. 4C).

Segmentation was likewise indistinguishable from expert annotation. Swell-versus-consensus Dice (0.92, 95% CI [0.87, 0.93]) was comparable to inter-annotator Dice (0.92, 95% CI [0.86, 0.93]); the paired difference was + 0.000 (95% CI [− 0.006, + 0.003]), within a ± 0.05 equivalence margin (Fig. 4D).

Propagation speed matched published values. The median SD event propagation speed was 41.5 μm/s (95% CI [39.0, 50.7]), falling well within the published range of 33–150 μm/s [1]. Additionally, this metric is consistent with the 45 μm/s (2.7 mm/min) reported for cortical SD in rat slices using IOSI [53] (Fig. 4E). Median relative neocortical area recruited was 72.2% of the neocortical ROI (Fig. 4F). Thus, Swell is a validated tool for detecting SD events and measuring their propagation speed, and it additionally quantifies the tissue area recruited.

3.3 Propagation of Halorhodopsin-Induced SD

IOS resolved SD initiated both during and after HaloR activation (Fig. 5A,B). Of SD events confirmed by DC electrophysiology, IOS detected 100% of events induced using elevated extracellular K^+ (n = 10 / 4 slices / 2 animals), 83% of events induced during HaloR activation (n = 18 / 11 slices / 8 animals), and 100% of events induced following HaloR activation (n = 4 / 4 slices / 4 animals) (Fig. 5C). Additionally, IOS detected 4 events during and 1 event following activation that were not captured by the recording electrode. The recording electrode was placed within the illuminated area, a location for which IOS are unresolvable at broad wavelengths. Detection by both electrophysiology and IOSI indicates tissue recruitment both within and outside the area of direct illumination, demonstrating clear propagation beyond the illuminated area.

HaloR-induced SD events propagate at a similar rate to SD events initiated via elevated extracellular K^+ (Fig. 5D). For SD detected by IOS, events initiating during illumination (n = 19 / 11 slices / 8 animals) had a median propagation speed of 43.9 μm/s (95% CI [41.7, 47.2]). Events that initiated post-illumination (n = 4 / 4 slices / 4 animals; one DC-confirmed event with multiple initiation sites excluded) had a median propagation speed of 47.8 μm/s (95% CI [41.3, 48.8]). Both medians are similar to the median propagation speed of extracellular K^+-induced SD events (41.5 μm/s, see 3.2), differing by + 2.4 μm/s for events during illumination (95% CI [− 6.6, + 7.4]) and + 6.3 μm/s for events post-illumination (95% CI [− 4.3, + 8.9]) (Fig. 5D). Each of these medians also falls within the published range of 33–150 μm/s [1]. Together, these Swell-derived measurements show that HaloR-induced SD events propagate beyond their illumination site at speeds comparable to those induced by elevated extracellular K^+.

4 Discussion

Characterizing IOS associated with SD has required labor-intensive analysis and lacked a standardized pipeline spanning induction methods. Swell addresses both in a single standalone application, and its agreement with expert annotation and DC electrophysiology shows that semi-automated analysis costs nothing in accuracy.

We have demonstrated that the amplitude of intensity changes alone does not effectively enable SD event detection. Thresholding on intensity change recovered nearly all real events but at a precision of 0.34, meaning two-thirds of its detections were artifacts (Fig. 3B). Adding a coherence gate that captures the slow, spatially progressive recruitment characteristic of SD raised precision to 0.80 at little cost in sensitivity (Fig. 3C). Distinguishing SD events from visual noise requires capturing the spatiotemporal characteristics of SD, alongside the magnitude of the intensity change.

Swell uses SAM 2.1, a foundation image segmentation model, to quantify SD. An earlier release of the same model was used to annotate IOS recordings of KCl-induced spreading depression *in vivo*, producing a preprocessed dataset [43]. Swell instead applies the model as the analysis engine of an end-to-end pipeline, pairing automated event detection with segmentation and metric export. Without any tuning on SD-specific training data, SAM 2.1 matched the expert annotators on *ex vivo* slice recordings, reproducing published SD event characteristics. This enables Swell to perform semi-automated segmentation for research groups without preexisting annotated SD datasets.

While SD can be recorded using electrophysiology, that approach alone is often insufficient. Limited spatial sampling cannot resolve the extent of SD spread and, at worst, misses events altogether. Our optogenetically induced SD data illustrate this, as they required both imaging and electrophysiology: the recording electrode necessarily sat inside the illuminated area, where IOS are unresolvable, while IOSI resolved the wavefront everywhere the electrode could not reach, capturing five events electrophysiology missed entirely. The blind spots of the two modalities fall in different places, making them complementary rather than redundant.

During these studies, we found HaloR-induced SD events to propagate consistently from their induction sites, which had not previously been shown with IOS, as prior recordings relied on electrophysiology alone [33]. Using Swell, we could reliably detect SD emerging during illumination, showing that optogenetically induced SD can be spatially mapped despite the strong, fluctuating light used to trigger them. Propagation beyond the illuminated area further establishes that these HaloR events carry the traveling wavefront that defines SD. They propagated at speeds in line with published ranges [53, 54] and similar to those we measured in our elevated extracellular K^+ recordings. That propagation speed did not detectably differ between events initiated under raised and reduced extracellular K^+ suggests that, once initiated, SD propagates similarly, regardless of the extracellular K^+ concentration at induction. This HaloR SD model can therefore aid in elucidating the mechanisms of both SD induction and propagation, an area of active research with diverse competing hypotheses [22, 34, 55].

A few limitations in our study must be acknowledged. The post-illumination dataset was relatively small (n = 4 animals; Fig. 5B,D). The cross-paradigm comparisons are descriptive without a formal equivalence test; optical intensity and area recruited were removed from analysis due to confounding from the intense illumination necessary for optogenetically induced SD. Swell is also semi-automated, requires user input at several stages, and, so far, has only been validated against *ex vivo* models.

Clear directions for future research include expanding Swell's application to *in vivo* models and use by other labs. Since IOSI does not require any dyes or genetic tools, this toolbox also has potential for use in human studies. Additional work could apply Swell to other models of SD induction, including channelrhodopsin paradigms, to generate a more comprehensive understanding of SD propagation mechanics. Full automation of SD analysis is a further goal: the annotated masks Swell produces could potentially be used to train a segmentation model that requires fewer or no user prompts, further reducing the manual analysis SD research currently demands.

5 Conclusions

In summary, we have shown the utility of Swell in *ex vivo* mouse models as a tool for identifying SD, characterizing key SD metrics, and integrating optogenetics, electrophysiology and IOS data. To our knowledge, Swell provides the first standalone desktop application for the detection and analysis of SD from IOSI, designed for use without programming experience or commercial software. Furthermore, we have demonstrated that HaloR-induced SD wavefronts propagate beyond the illuminated region at speeds comparable to those of SD induced by elevated extracellular K^+, establishing the HaloR model as a reliable tool for characterizing both SD initiation and propagation and for determining the mechanistic similarities and differences between these processes. In addition to SD applications, Swell's open-source code and general analysis features make it adaptable to other physiological research contexts that utilize IOSI.

Abbreviations

SD
spreading depolarization
IOSI
intrinsic optical signal imaging
IOS
intrinsic optical signals
HaloR
halorhodopsin
SAM
Segment Anything Model
IACUC
Institutional Animal Care and Use Committee
aCSF
artificial cerebrospinal fluid
DC
direct current
ROI

region of interest
MAD
median absolute deviation
CI
confidence interval

Declarations

Ethics Approval and Consent to Participate

All research processes were conducted in accordance with ARRIVE guidelines [56]. All animal procedures were performed under the supervision of and in accordance with Brigham Young University IACUC guidelines (protocol #25–0715).

Consent for Publication

Not applicable.

Competing Interests

The authors declare that they have no competing interests.

Funding

This work was funded by the Brain Research Foundation and the BYU College of Life Sciences. The funders had no role in study design, data collection and analysis, decision to publish, or preparation of the manuscript.

Author Contribution

C.D. contributed toward conceptualization, formal analysis, tool methodology, project administration, Swell software development, figure creation, and manuscript writing, editing, and reviewing. P.W. contributed toward data curation, investigation, validation, and writing the original draft. D.N. and T.S. contributed toward data curation, investigation, experimental methodology, validation, and reviewing and editing the manuscript. R.P. contributed toward project conceptualization, funding acquisition, project administration, resources, supervision, and reviewing and editing the manuscript. All authors read and approved the final manuscript.

Acknowledgement

We sincerely thank Dr. Juha Voipio for his generous donations of lab equipment that made this work possible, and Rachel Ricks and Tyler Poulos for their feedback and writing assistance.

Data Availability

The datasets generated and analyzed during the current study are not publicly available because they form part of an ongoing study and will be analyzed alongside currently unpublished work but are available from the corresponding author on reasonable request.

References

1. Somjen GG (2001) Mechanisms of spreading depression and hypoxic spreading depression-like depolarization. Physiol Rev 81(3):1065–1096. 10.1152/physrev.2001.81.3.1065
2. Leão AAP (1944) Spreading Depression of Activity in the Cerebral Cortex. J Neurophysiol 7(6):359–390. 10.1152/jn.1944.7.6.359
3. Chever O, Zerimech S, Scalmani P, Lemaire L, Pizzamiglio L, Loucif A, Ayrault M, Krupa M, Desroches M, Duprat F, Léna I, Cestèle S, Mantegazza M (2021) Initiation of migraine-related cortical spreading depolarization by hyperactivity of GABAergic neurons and NaV1.1 channels. J Clin Invest 131(21). 10.1172/JCI142203
4. Noseda R, Burstein R (2013) Migraine pathophysiology: anatomy of the trigeminovascular pathway and associated neurological symptoms, cortical spreading depression, sensitization, and modulation of pain. Pain 154:S44–S53. 10.1016/j.pain.2013.07.021
5. Charles AC, Baca SM (2013) Cortical spreading depression and migraine. Nat Rev Neurol 9(11):637–644. 10.1038/nrneurol.2013.192
6. Norby JH, Hummel D, Ricks N, Rolston J, Rahimpour S, Cowan R, Voipio J, Trevelyan AJ, Smith EH, Parrish RR (2025) Rodent and human seizures demonstrate a dynamic interplay with spreading depolarizations. Neurobiol Dis 211:106937. 10.1016/j.nbd.2025.106937
7. Kramer DR, Fujii T, Ohiorhenuan I, Liu CY (2016) Cortical spreading depolarization: Pathophysiology, implications, and future directions. J Clin Neurosci 24:22–27. 10.1016/j.jocn.2015.08.004
8. Tamim I, Chung DY, de Morais AL, Loonen IC, Qin T, Misra A, Schlunk F, Endres M, Schiff SJ, Ayata C (2021) Spreading depression as an innate antiseizure mechanism. Nat Commun 12(1):2206. 10.1038/s41467-021-22464-x
9. Mosley N, Chung JY, Jin G, Franceschini MA, Whalen MJ, Chung DY (2022) Cortical spreading depolarization, blood flow, and cognitive outcomes in a closed head injury mouse model of traumatic brain injury. Neurocrit Care 37(Suppl 1):102–111. 10.1007/s12028-022-01474-7

10. Dreier JP, Fabricius M, Ayata C, Sakowitz OW, Shuttleworth CW, Dohmen C, Graf R, Vajkoczy P, Helbok R, Suzuki M (2017) Recording, analysis, and interpretation of spreading depolarizations in neurointensive care: review and recommendations of the COSBID research group. J Cereb Blood Flow Metab 37(5):1595–1625. 10.1177/0271678X16654496
11. van Hameren G, Aboghazleh R, Parker E, Dreier JP, Kaufer D, Friedman A (2024) From spreading depolarization to blood–brain barrier dysfunction: navigating traumatic brain injury for novel diagnosis and therapy. Nat Rev Neurol 20(7):408–425. 10.1038/s41582-024-00973-9
12. Törteli A, Tóth R, Berger S, Samardzic S, Bari F, Menyhárt Á, Farkas E (2023) Spreading depolarization causes reperfusion failure after cerebral ischemia. J Cereb Blood Flow Metab 43(5):655–664. 10.1177/0271678X231153745
13. Ayata C, Lauritzen M (2015) Spreading depression, spreading depolarizations, and the cerebral vasculature. Physiol Rev 95(3):953–993. 10.1152/physrev.00027.2014
14. Dreier JP, Reiffurth C (2015) The stroke-migraine depolarization continuum. Neuron 86(4):902–922. 10.1016/j.neuron.2015.04.004
15. Ricks R, Bawuah Afran-Okese K, Withers PC, Shafer TL, Roque I, Poulos T, Norby JH, Maxfield R, Parrish RR (2026) Cellular and network mechanisms of spreading depolarization. Adv Physiol Educ 50(3):929–941. 10.1152/advan.00201.2025
16. Vinogradova LV, Rysakova MP, Pavlova IV (2020) Small damage of brain parenchyma reliably triggers spreading depolarization. Neurol Res 42(1):76–82. 10.1080/01616412.2019.1709745
17. Akerman S, Holland PR, Goadsby PJ (2008) Mechanically-induced cortical spreading depression associated regional cerebral blood flow changes are blocked by Na + ion channel blockade. Brain Res 1229:27–36. 10.1016/j.brainres.2008.07.014
18. Holland P, Akerman S, Goadsby P (2010) Cortical spreading depression-associated cerebral blood flow changes induced by mechanical stimulation are modulated by AMPA and GABA receptors. Cephalalgia 30(5):519–527. 10.1111/j.1468-2982.2009.02021.x
19. Müller M, Somjen GG (1999) Intrinsic optical signals in rat hippocampal slices during hypoxia-induced spreading depression-like depolarization. J Neurophysiol 82(4):1818–1831. 10.1152/jn.1999.82.4.1818
20. Mané M, Müller M (2012) Temporo-spectral imaging of intrinsic optical signals during hypoxia-induced spreading depression-like depolarization. PLoS ONE 7(8):e43981. 10.1371/journal.pone.0043981
21. Pietrobon D, Moskowitz MA (2014) Chaos and commotion in the wake of cortical spreading depression and spreading depolarizations. Nat Rev Neurosci 15(6):379–393. 10.1038/nrn3770
22. Andrew RD, Hartings JA, Ayata C, Brennan K, Dawson-Scully KD, Farkas E, Herreras O, Kirov SA, Müller M, Ollen-Bittle N (2022) The critical role of spreading depolarizations in early brain injury: consensus and contention. Neurocrit Care 37(Suppl 1):83–101. 10.1007/s12028-021-01431-w
23. Juzekaeva E, Gainutdinov A, Mukhtarov M, Khazipov R (2020) Reappraisal of anoxic spreading depolarization as a terminal event during oxygen–glucose deprivation in brain slices in vitro. Sci Rep

10(1):18970. 10.1038/s41598-020-75975-w

24. Dreier JP (2011) The role of spreading depression, spreading depolarization and spreading ischemia in neurological disease. Nat Med 17(4):439–447. 10.1038/nm.2333
25. Hartings JA, Shuttleworth CW, Kirov SA, Ayata C, Hinzman JM, Foreman B, Andrew RD, Boutelle MG, Brennan K, Carlson AP (2017) The continuum of spreading depolarizations in acute cortical lesion development: examining Leao's legacy. J Cereb Blood Flow Metab 37(5):1571–1594. 10.1177/0271678X16654495
26. Herreras O, Somjen GG (1993) Analysis of potential shifts associated with recurrent spreading depression and prolonged unstable spreading depression induced by microdialysis of elevated K + in hippocampus of anesthetized rats. Brain Res 610(2):283–294. 10.1016/0006-8993(93)91412-I
27. Withers PC, Jones A, Afran-Okese KB, Calder B, Morrill HJ, Shafer TL, Nevers DS, Norby JH, Acosta R, Bikman BT, Suli A, Parrish RR (2025) Pharmacological inhibition of all known major inward cationic currents does not block the induction of spreading depolarizations. Front Cell Neurosci 19:1668329. 10.3389/fncel.2025.1668329
28. Anderson TR, Andrew RD (2002) Spreading depression: imaging and blockade in the rat neocortical brain slice. J Neurophysiol 88(5):2713–2725. 10.1152/jn.00321.2002
29. Andrew RD, Hsieh Y-T, Brisson CD (2017) Spreading depolarization triggered by elevated potassium is weak or absent in the rodent lower brain. J Cereb Blood Flow Metab 37(5):1735–1747. 10.1177/0271678X16657344
30. Houben T, Loonen IC, Baca SM, Schenke M, Meijer JH, Ferrari MD, Terwindt GM, Voskuyl RA, Charles A, van den Maagdenberg AM (2017) Optogenetic induction of cortical spreading depression in anesthetized and freely behaving mice. J Cereb Blood Flow Metab 37(5):1641–1655. 10.1177/0271678X16645113
31. Sugimoto K, Yang J, Fischer P, Takizawa T, Mulder IA, Qin T, Erdogan TD, Yaseen MA, Sakadžić S, Chung DY (2023) Optogenetic spreading depolarizations do not worsen acute ischemic stroke outcome. Stroke 54(4):1110–1119. 10.1161/STROKEAHA.122.041351
32. Mitlasóczki B, Gutiérrez Gómez A, Kamali M, Babushkina N, Baues M, Kück L, Haubrich AN, Tamiolakis T, Breuer A, Granak S (2025) Hippocampal spreading depolarization as a driver of postictal ambulation. Sci Transl Med 17(816):eadv3260. 10.1126/scitranslmed.adv3260
33. Parrish RR, MacKenzie-Gray Scott C, Jackson-Taylor T, Grundmann A, McLeod F, Codadu NK, Călin A, Alfonsa H, Wykes RC, Voipio J (2023) Indirect effects of halorhodopsin activation: potassium redistribution, nonspecific inhibition, and spreading depolarization. J Neurosci 43(5):685–692. 10.1523/JNEUROSCI.1141-22.2022
34. Ricks R, Scott CMG, Trevelyan AJ, Parrish RR (2025) Mechanistic insight into the initiation of spreading depolarizations: Is it really all about potassium? J Physiol 603(11):3269. 10.1113/JP288809
35. Ayata C (2013) Pearls and pitfalls in experimental models of spreading depression. Cephalalgia 33(8):604–613. 10.1177/0333102412470216

36. Aitken PG, Tombaugh GC, Turner DA, Somjen GG (1998) Similar Propagation of SD and Hypoxic SD-Like Depolarization in Rat Hippocampus Recorded Optically and Electrically. J Neurophysiol 80(3):1514–1521. 10.1152/jn.1998.80.3.1514
37. Chen S, Li P, Luo W, Gong H, Cheng H (2003) Luo Q In vivo optical imaging of cortical spreading depression in rat. In: Third International Conference on Photonics and Imaging in Biology and Medicine, SPIE, p 262. 10.1117/12.546172
38. Yoon R, Tsang P, Lenz F, Kwan H (1996) Characterization of cortical spreading depression by imaging of intrinsic optical signals. NeuroReport 7(15):2671–2674. 10.1097/00001756-199611040-00052
39. Kawauchi S, Sato S, Uozumi Y, Nawashiro H, Ishihara M, Ashida H (2012) Control of anoxic depolarization in rat brain by near-infrared laser irradiation and its monitoring by intrinsic optical signal imaging. Mechanisms for Low-Light Therapy VII. SPIE, pp 71–76
40. Lu Y-L, Scharfman HE (2021) New Insights and Methods for Recording and Imaging Spontaneous Spreading Depolarizations and Seizure-Like Events in Mouse Hippocampal Slices. Front Cell Neurosci 15:761423. 10.3389/fncel.2021.761423
41. Yan H Yan Q An innovative software for data analysis of the intrinsic signals of optical imaging. In: 2010 3rd International Congress on Image and Signal Processing, 2010. IEEE, pp 85–88
42. Vasquez B, Campos B, Cao A, Theint Theint A, Zeiger W (2023) High-sensitivity intrinsic optical signal imaging through flexible, low-cost adaptations of an upright microscope. eNeuro 10 (8):ENEURO.0046-23.2023. 10.1523/ENEURO.0046-23.2023
43. Zhang W, Zeng G, Zheng Z, Li H, Qin W, Lv J (2026) A Mouse Cortex Video Segmentation Dataset for Intrinsic Optical Signal Tracking and Neural Activity Analysis. Sci Data 13(1):255. 10.1038/s41597-026-06580-1
44. Dunford C (2026) Swell Source Code Repository. https://github.com/ParrishLab/Swell. Accessed 27 August 2026
45. Ravi N, Gabeur V, Hu Y-T, Hu R, Ryali C, Ma T, Khedr H, Rädle R, Rolland C (2025) Gustafson L SAM 2: Segment anything in images and videos. In: International Conference on Learning Representations, pp 28085–28128
46. Gorski JA, Talley T, Qiu M, Puelles L, Rubenstein JL, Jones KR (2002) Cortical excitatory neurons and glia, but not GABAergic neurons, are produced in the Emx1-expressing lineage. J Neurosci 22(15):6309–6314. 10.1523/JNEUROSCI.22-15-06309.2002
47. Withers PC, Morrill HJ, Parrish RR (2024) An Open-Source 3D–Printed Recording Stage with Customizable Chambers for Ex Vivo Experiments. eNeuro 11 (9):ENEURO.0257-24.2024. 10.1523/eneuro.0257-24.2024
48. Withers PC (2025) A 3D-printed interface holding chamber for mouse brain slice electrophysiology. 10.5281/zenodo.16942955. Zenodo
49. Taylor AL, Ackerman DG, Arthur BJ, Iyer V, Edson P, Spruston N, Svoboda K (2022) WaveSurfer. 10.5281/zenodo.15103514

50. Fayuk D, Aitken PG, Somjen GG, Turner DA (2002) Two Different Mechanisms Underlie Reversible, Intrinsic Optical Signals in Rat Hippocampal Slices. J Neurophysiol 87(4):1924–1937. 10.1152/jn.00231.2001
51. Harris CR, Millman KJ, Van Der Walt SJ, Gommers R, Virtanen P, Cournapeau D, Wieser E, Taylor J, Berg S, Smith NJ (2020) Array programming with NumPy. Nature 585(7825):357–362. 10.1038/s41586-020-2649-2
52. Virtanen P, Gommers R, Oliphant TE, Haberland M, Reddy T, Cournapeau D, Burovski E, Peterson P, Weckesser W, Bright J (2020) SciPy 1.0: fundamental algorithms for scientific computing in Python. Nat Methods 17(3):261–272. 10.1038/s41592-019-0686-2
53. Buchheim K, Weissinger F, Siegmund H, Holtkamp M, Schuchmann S, Meierkord H (2002) Intrinsic optical imaging reveals regionally different manifestation of spreading depression in hippocampal and entorhinal structures in vitro. Exp Neurol 175(1):76–86. 10.1006/exnr.2002.7893
54. Fujita S, Mizoguchi N, Aoki R, Cui Y, Koshikawa N, Kobayashi M (2016) Cytoarchitecture-dependent decrease in propagation velocity of cortical spreading depression in the rat insular cortex revealed by optical imaging. Cereb Cortex 26(4):1580–1589. 10.1093/cercor/bhu336
55. Kim D, Gagolewicz P, McQueen S, Latour H, Tresidder K, Jarvis CR, Andrew RD (2025) Simulated ischemia in live cerebral slices is mimicked by opening the Na+/K+ pump: clues to the generation of spreading depolarization. J Neurophysiol 133(6):1649–1664. 10.1152/jn.00429.2024
56. Percie du Sert N, Hurst V, Ahluwalia A, Alam S, Avey MT, Baker M, Browne WJ, Clark A, Cuthill IC, Dirnagl U (2020) The ARRIVE guidelines 2.0: Updated guidelines for reporting animal research. J Cereb Blood Flow Metab 40(9):1769–1777. 10.1177/0271678X20943823
57. Dunford C (2026) Swell: intrinsic optical signal imaging analysis for spreading depolarization event identification and segmentation (version 0.3.7). 10.5281/zenodo.22033534. Zenodo
58. Parrish RR (2026) Experimental and analytical workflow for detecting and quantifying spreading depolarization from intrinsic optical signals. BioRender. https://BioRender.com/8xd2jgr

Figures

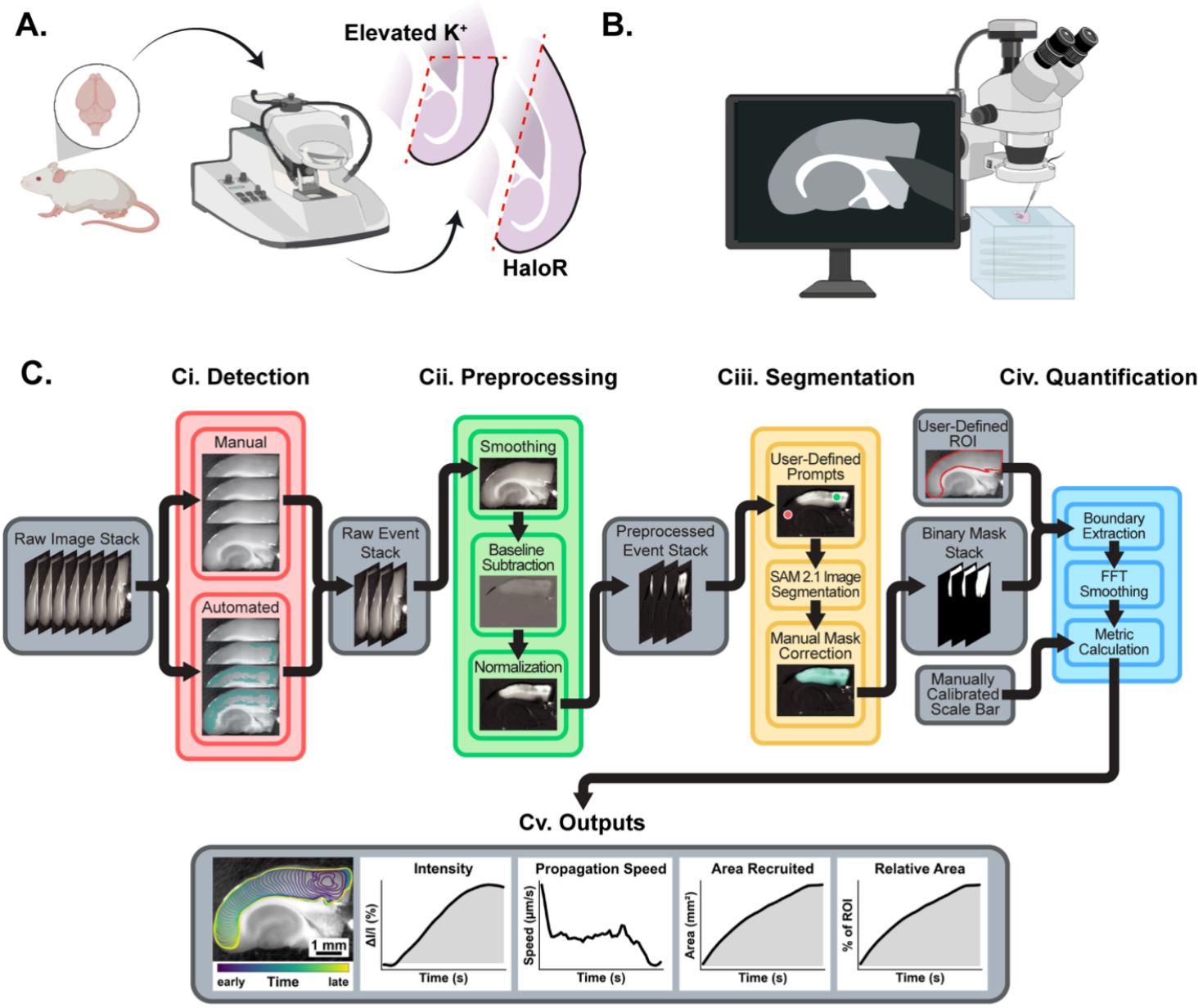


Figure 1

Experimental and analytical workflow for detecting and quantifying spreading depolarization from intrinsic optical signals. (**A**) Preparation of mouse brain slices, demonstrating the two cut schemes for elevated extracellular K^+ and halorhodopsin (HaloR) paradigms. (**B**) Experimental setup showing brain slices placed on an interface recording chamber. A microelectrode is inserted into the slice for simultaneous direct current recording and intrinsic optical signal (IOS) imaging during spreading depolarization (SD). (**C**) A raw IOS image stack is processed through Swell's four stages (**Ci–Civ**) to yield quantitative metrics of SD propagation (**Cv**). (**Ci**) Candidate events are detected manually or automatically using a two-stage detector. (**Cii**) Each detected event clip is smoothed, baseline-subtracted, and normalized to isolate the SD-related signal. (**Ciii**) The user prompts a SAM 2.1

segmentation model, followed by optional manual correction, to produce a per-frame binary mask stack of the wavefront. (**Civ**) For event quantification, each binary mask is intersected with a user-defined region of interest (ROI), and the resulting wavefront boundary is extracted, smoothed with a fast Fourier transform low-pass filter, scaled to physical units using a manually calibrated scale bar, and converted to propagation metrics. (**Cv**) Representative outputs for one event: a time-colored wavefront contour map and time series of signal intensity ($\Delta I/I_0$), propagation speed (μm/s), absolute area recruited (mm^2), and area relative to the ROI (%). Created in BioRender [58].

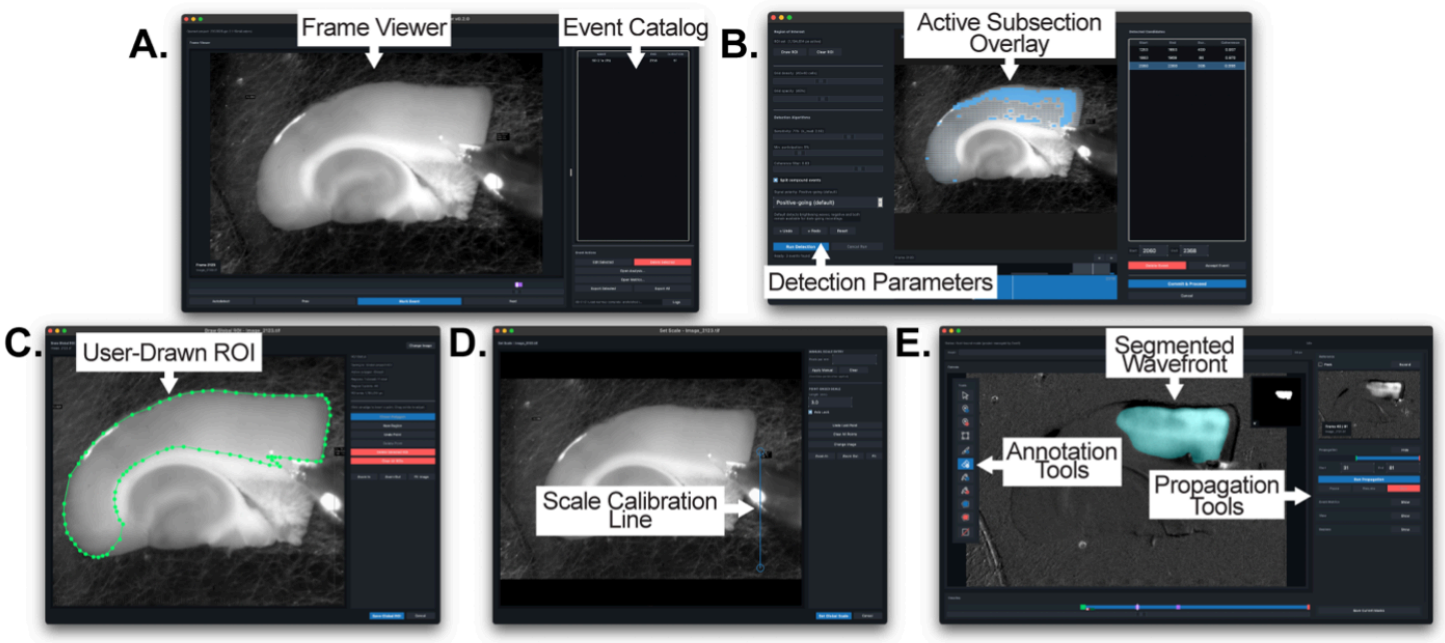


Figure 2

Swell's graphical user interface. Swell is an open-source desktop application that enables the detection, segmentation, and quantification of spreading depolarizations (SD). (**A**) The primary window where image stacks are loaded and displayed in the frame viewer; the user navigates through frames and manually marks SD events, adding them to the event catalog for analysis. (**B**) The automated detection window where the user defines detection parameters and runs the detector; the resulting active-subsection overlay (blue) allows the user to visualize SD recruited slice subsections and manually distinguish true events from false positives among the candidate events. (**C**) The user defines a region of interest (ROI, green) by drawing a polygon. (**D**) The user draws a scale calibration line and enters its length in millimeters, allowing Swell to convert pixel distances to physical units. (**E**) The analysis window where annotation tools are used to place prompts and manually correct masks; the user can run and configure the SAM 2.1 model to generate and track the wavefront mask across frames. The segmented wavefront (cyan) shows the current mask, combining model segmentation with manual correction.

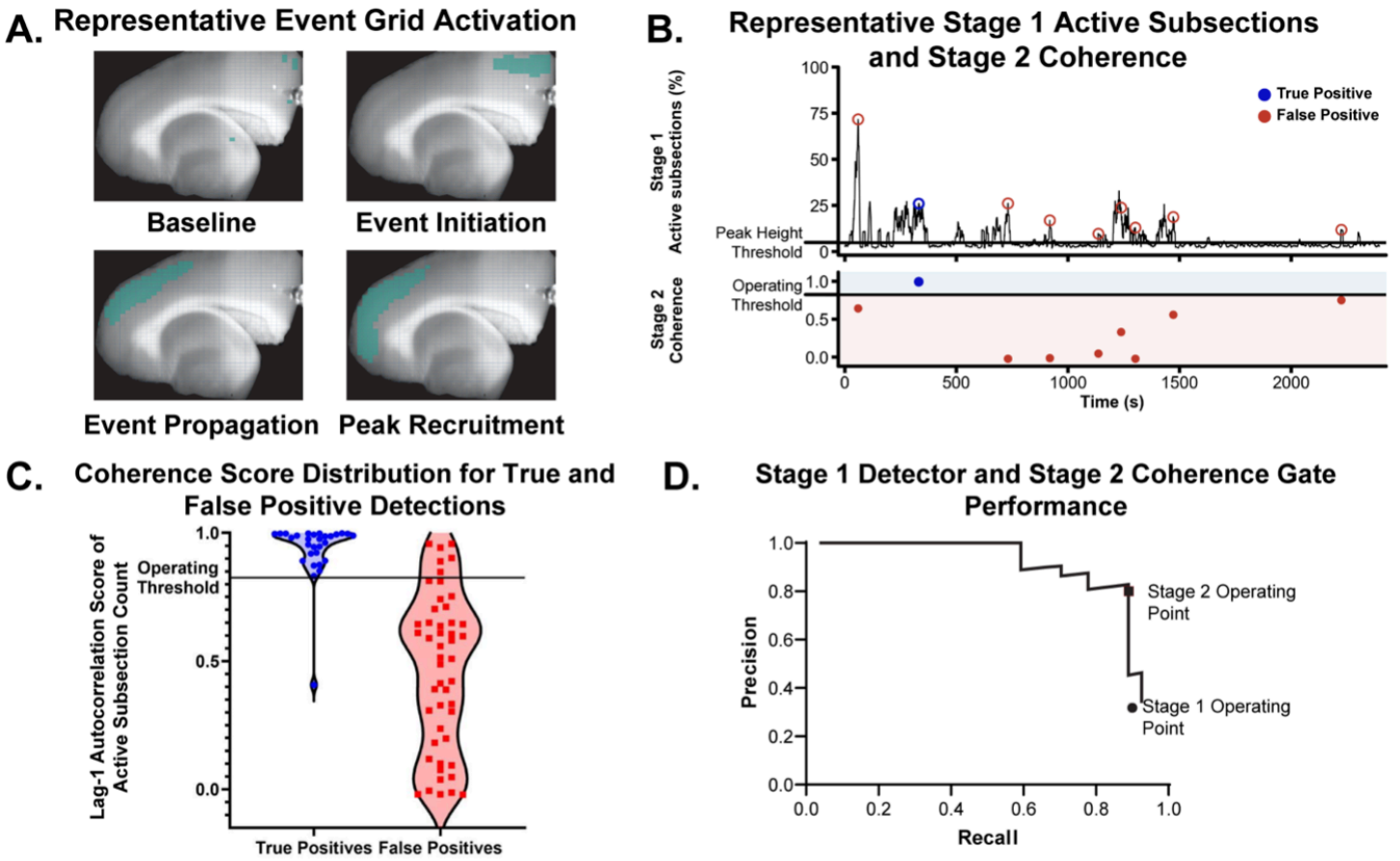


Figure 3

Two-stage automated detection of spreading depolarization (SD). Detector performance was evaluated on 27 SD events across 10 slices from 7 animals (15 and 26 mM K^+) using leave-one-animal-out cross-validation. **(A)**Representative grid activation for one detected SD event. Each detector subsection in the 40 × 40 grid is shaded when active, shown at four representative timepoints: baseline, event initiation, propagation, and peak recruitment. **(B)**Detection signal for the representative recording. Top: the Stage 1 trace, the percentage of active subsections per frame; candidates exceeding the Stage 1 peak-height threshold (5% of retained subsections) are circled and colored by outcome. Bottom: Stage 2 coherence score for each candidate, with the operating threshold (0.826) marked. The tallest Stage 1 peak is a movement/perfusion artifact that the coherence gate rejects, whereas the true SD (lower amplitude) is retained. **(C)** Distribution of Stage 2 coherence scores (lag-1 autocorrelation of the active-subsection-count signal) for true-positive versus false-positive candidates. The operating threshold marks where the detector separates retained events from rejected ones. **(D)** Precision–recall performance. Stage 1 alone recovered 25/27 events but produced 49 false-positive windows; adding the Stage 2 coherence gate reduced false positives to 6 while retaining 24/27 events, yielding an overall precision of 0.80 (95% CI [0.73, 0.90]) and recall of 0.89 (95% CI [0.82, 0.96]). Operating points for both stages are indicated.

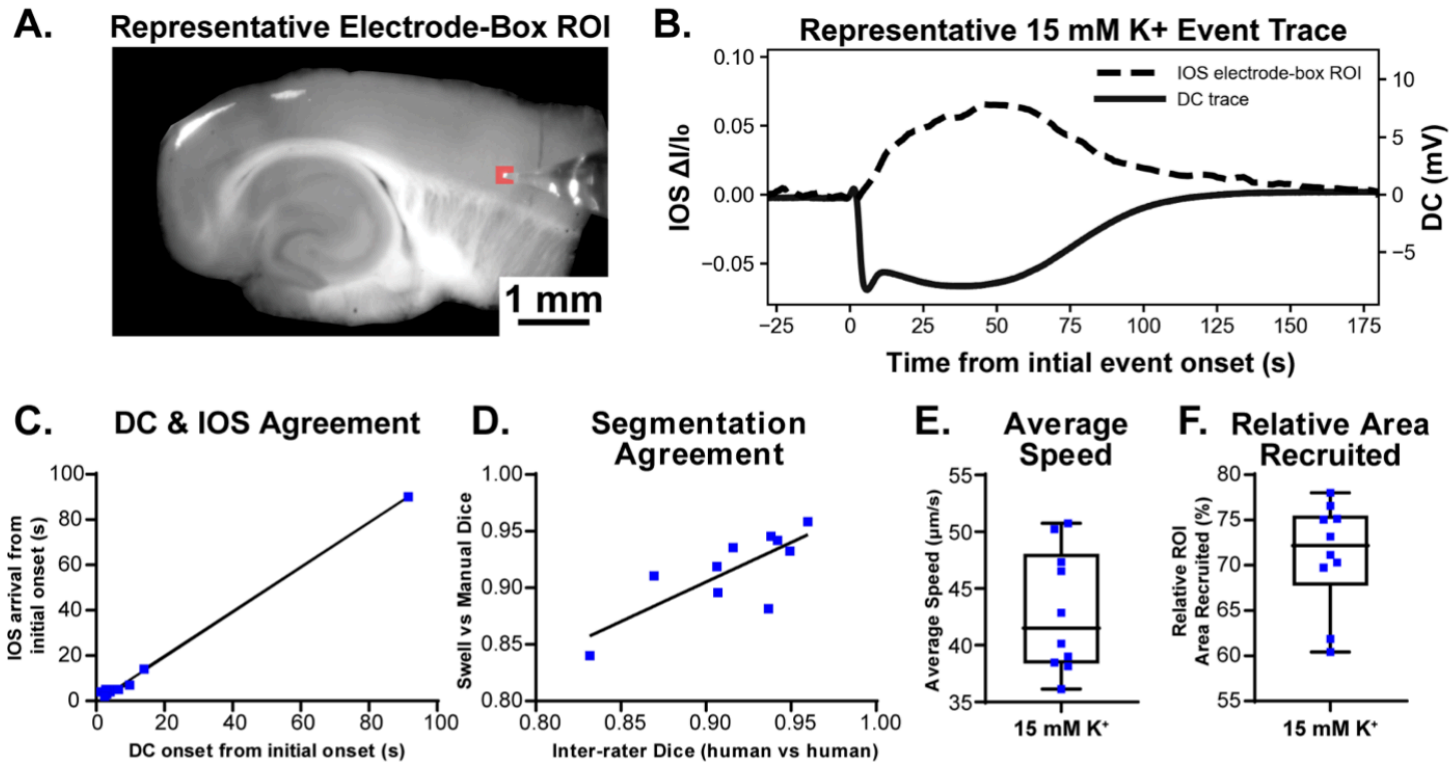


Figure 4

Validation of Swell against simultaneous electrophysiology and manual annotation. All data are 15 mM elevated extracellular K^+-induced, single-initiation site spreading depolarization (SD) events (n = 10 / 4 slices / 2 animals). **(A)** Representative recording field showing the electrode-box region of interest (ROI, red) — a 100 × 100 pixel box centered on the recording-electrode tip, over the slice from which the intrinsic optical signal (IOS) time series was extracted. **(B)** Representative simultaneously acquired traces for one event: the IOS signal from the electrode ROI ($\Delta I/I_0$, dashed; baseline from the 30 s preceding direct current (DC) shift) and the co-localized DC potential (solid), aligned to initial event onset; smoothed for display. **(C)** Timing agreement between IOS arrival and DC shift, each expressed relative to initial event onset. No systematic offset was found (bias −0.2 s, slice-clustered 95% CI [−2.2 s, +0.3 s]); all 10/10 IOS arrivals fell within 3 s of the DC shift (median absolute difference 1 s). **(D)** Segmentation agreement: Dice overlap between Swell and the manual consensus (majority vote of three blinded annotators) versus inter-annotator Dice. Swell-versus-consensus agreement (0.92, 95% CI [0.87, 0.93]) matched inter-annotator agreement (0.92, 95% CI [0.86, 0.93]); paired difference +0.000 (95% CI [−0.006, +0.003]), within a ±0.05 equivalence margin. **(E)** Per event propagation speed: median 41.5 μm/s (IQR [38.6, 47.1]; range [36.1, 50.7]), within the published 33–150 μm/s range. **(F)** Maximum relative neocortical area recruited: median 72.2% (IQR [69.9, 75.1]; range [60.4, 78.0]).

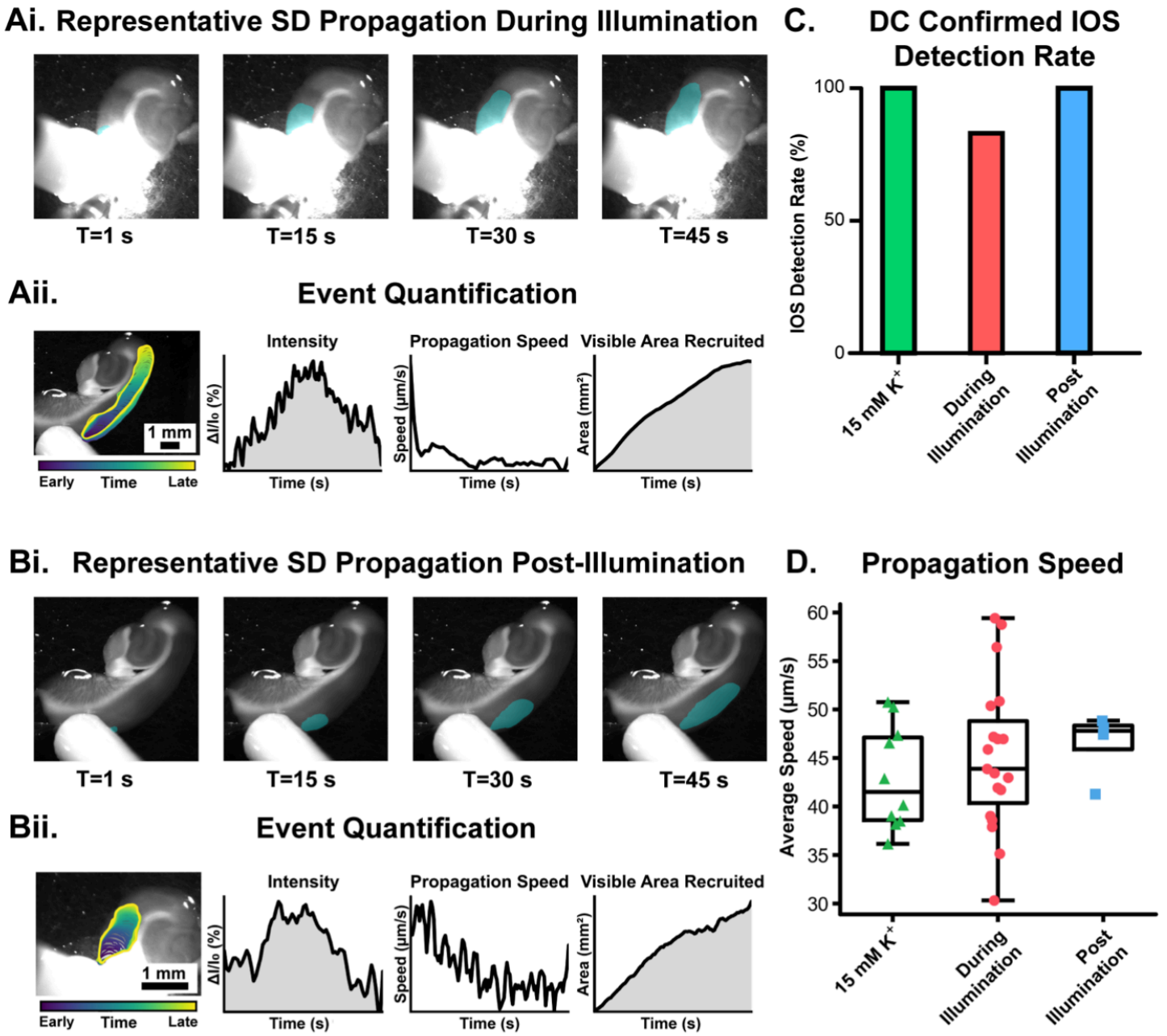


Figure 5

Swell characterizes Halorhodopsin-induced spreading depolarization (SD) during and after illumination. Events were classified by onset timing relative to 565 nm illumination (during or within 30 s after). **(Ai)**Representative SD propagating during illumination, shown as the Swell-segmented wavefront (teal) at four timepoints. **(Aii)** Quantification of the same event: a time-colored wavefront contour map with per-frame intensity, propagation speed, and visible area recruited. Intensity and area are shown for illustration only; both were excluded from grouped analysis because optical activation confounds these measures. **(Bi, Bii)** As in Ai–Aii, for a representative SD initiating post-illumination. **(C)** The proportion of SD events confirmed by electrophysiology (direct current shift) that were also detected by intrinsic optical signals (IOS). IOS detected 100% of 15 mM K^+ events (n = 10 / 4 slices / 2 animals), 83% of

during-illumination events (n = 18 / 11 slices / 8 animals), and 100% of post-illumination events (n = 4 / 4 slices / 4 animals). IOS additionally detected 4 events during and 1 post-illumination event not captured by the electrode (placed within the illuminated area, where IOS are unresolvable), indicating recruitment beyond the directly illuminated region. **(D)** Propagation speed by paradigm. During illumination: median 43.9 µm/s (95% CI [41.7, 47.2]; IQR [40.4, 48.8]; range [30.3, 59.4]; n = 19 events / 11 slices / 8 animals). Post-illumination: median 47.8 µm/s (95% CI [41.3, 48.8]; IQR [45.9, 48.3]; range [41.3, 48.8]; n = 4 / 4 slices / 4 animals). 15 mM K^+: median 41.5 µm/s (95% CI [39.0, 50.7]; IQR [38.6, 47.1]; range [36.1, 50.7]; n = 10 / 4 slices / 2 animals). All three medians fall within the published 33–150 µm/s range.

Supplementary Files

This is a list of supplementary files associated with this preprint. Click to download.

- ArriveAuthorChecklist.pdf